International Journal of Solids and Structures 45 (2008) 4648–4661

Contents lists available at ScienceDirect

International Journal of Solids and Structures

journal homepage: www.elsevier.com/locate/ijsolstr

Modelling of compressive behaviour of concrete-like materials at high strain rate

X.Q. Zhou *, H. Hao

School of Civil & Resource Engineering, The University of Western Australia, 35 Stirling Highway, Crawley, Perth, WA 6009, Australia

ARTICLE INFO

Article history:
Received 12 December 2007
Received in revised form 10 March 2008
Available online 22 April 2008

Keywords:
Mesoscale model
Concrete-like material
Numerical simulation
High strain rate
Compressive strength

ABSTRACT

Uniaxial compression tests are the most common tests for characterizing the strength of concrete-like materials. The dynamic compression strength of concrete-like material is typically obtained by Split Hopkinson Pressure Bar (SHPB) tests. The increase in material strength under dynamic loading is usually attributed to the strain rate effect and modelled with a dynamic increase factor (DIF). However, it was observed by some researchers that the radial inertial confinement caused apparent increase of dynamic strength of concrete-like specimen in SHPB tests. They attributed the material strength increase to this inertial effect, instead of the strain rate effect. In the present study, numerical analyses are performed to investigate the compressive behaviour of concrete-like material at high strain rates. A homogeneous macroscale model and a heterogeneous mesoscale model are developed in the study. In the macroscale model, the material is assumed to be homogeneous and isotropic. In the mesoscale model, the test sample is modelled as a three-phase composite consisting of aggregate, mortar matrix and interfacial transaction zone (ITZ) between the aggregate and the mortar matrix. The aggregate is assumed to be circular and the ITZ is modelled as a thin boundary around the aggregate. In the both models, the materials are assumed to be insensitive to the strain rate first. Therefore, the obtained strength enhancement is only due to the inertial confinement. Strain rate sensitive material properties are then used in the two models in the calculations. Numerical simulations of the concrete samples under compression at different strain rates are carried out. The relative contribution of the inertial effect and the strain rate effect on the compressive strength DIF is examined based on the numerical results. The failure process of concrete specimen is also studied.

1. Introduction

As one of the most commonly used construction materials, concrete may be subjected to extreme dynamic loads such as blast loads and high velocity impact loads. Understanding the response of concrete specimens subjected to high strain rate deformation is essential to grasp the behaviour of concrete structures under the extreme loading cases. Uniaxial compression tests are the most common methods for characterizing the strength of concrete, as well as concrete-like composite materials. The direct compression Split Hopkinson Pressure Bar (SHPB) technique (Kolsky, 1949) is a popular way to measure the dynamic compression strength enhancement of concrete-like materials at high strain rate. Extensive experimental results have shown that the dynamic uniaxial compressive strength increased with the increase of the strain rate (Bischoff and Perry, 1991; Ross et al., 1989; Grote et al., 2001; Tedesco et al., 1994; Georgin and Reynouard, 2003; Li and Meng, 2003). Typically,

* Corresponding author. Tel.: +61 8 64887357; fax: +61 8 64881044.
E-mail address: xzhou@civil.uwa.edu.au (X.Q. Zhou).

0020-7683/$ - see front matter © 2008 Elsevier Ltd. All rights reserved.
doi:10.1016/j.ijsolstr.2008.04.002

the dynamic increase factor (DIF), defined by the ratio of the dynamic strength to the static strength of the material, is used to model the strength enhancement by the strain rate effect. Based on experimental results, some empirical compressive DIF formulae were developed. For example, CEB recommendation (Comite Euro-International du Beton, 1993), Tedesco and Ross's empirical DIF (Tedesco and Ross, 1998), Grote's compressive DIF (Grote et al., 2001), and the DIF adopted in the concrete model in Katayama's work (Katayama et al., 2007). However, this phenomenon is still not well understood. The only well accepted idea is that, two factors, namely the viscoelastic character of the hardened cement paste and the time-dependent micro-crack growth, may contribute to the high strain rate effect. Some researchers argued that the increase of dynamic uniaxial strength is only caused by the inertial confinement (Ma et al., 2006; Cotsovos and Pavlović, 2007). Other researchers found that the increase of dynamic compressive strength could be only caused by the inertial confinement when the strain rate is higher than around $10^2\ s^{-1}$ (Li and Meng, 2003). However, most of the available empirical formulae for DIF are mainly curve-fitting of the dynamic experimental results regardless of the inertial confinement. In this consideration, the available DIFs might overestimate the dynamic compressive strength of concrete and concrete-like materials.

To analyse the strength enhancement caused by the inertial confinement and to compare the differences of the strain rate insensitive/sensitive models, a piece-wise linear Drucker–Prager concrete material model together with the commercial software AUTODYN (2005) is used to simulate the dynamic compressive behaviour of concrete-like material specimens. In the present study, a detailed model including the pressure bars and specimen and a simplified model with only the specimen are developed to simulate the SHPB test and the results are compared; then the simplified model is adopted to calculate the dynamic compressive behaviour of the specimen under different strain rates. In numerical simulation, two different models, i.e, a macroscale homogeneous model and a mesoscale heterogeneous model, are used. Firstly the strain rate effect is not considered in either model of the concrete-like specimen. Thus the enhancement of the dynamic strength is only caused by the inertial confinement. Similar methodology can be found in Li and Meng (2003). Next the strain rate sensitive material model is used to simulate the concrete-like material. The results from the strain rate sensitive/insensitive models are compared, and the contribution of the inertial confinement to the DIF obtained from both the homogeneous and mesoscale models are analysed.

2. SHPB technique

The SHPB test set-up is shown in Fig. 1 (Tedesco et al., 1994). The system consists of a striker bar (which is propelled by a gas gun), an incident pressure bar, a transmitter pressure bar and a short material specimen sandwiched between them. The loading compressive stress wave is initiated by the impact of the striker bar on the incident bar. The incident stress wave travels along the bar and is recorded at the strain gauge A. When the stress wave reaches the interface between the incident bar and the specimen, it is partially reflected at the interface and partially transmitted to the specimen. The reflected stress wave can also be recorded by the strain gauge A on the incident bar. At the interface between the specimen and the transmitted bar, the stress wave is again partially reflected and partially transmitted. The strain gauge B records the transmitted stress wave in the transmitter bar.

The boundary condition of the specimen is shown in Fig. 2 (Georgin and Reynouard, 2003). According to the one-dimensional stress wave theory,

$$F_1 = AE(\varepsilon_i + \varepsilon_r) \tag{1}$$

$$F_2 = AE(\varepsilon_t) \tag{2}$$

$$V_1 = C(\varepsilon_i - \varepsilon_r) \tag{3}$$

$$V_2 = C(\varepsilon_t) \tag{4}$$

where A is the cross-section area of the elastic pressure bars, i.e., incident and transmitter bars; E is the Young's modulus of the bar, $C = \sqrt{E/\rho}$, is the wave velocity in the bar, ρ is the density of the bar; ε_i and ε_r are the incident strain wave and the

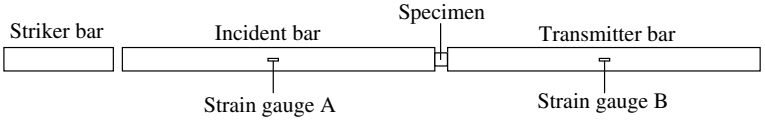

Fig. 1. SHPB test set-up.

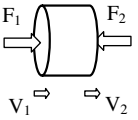

Fig. 2. Boundary condition of the specimen.

reflected strain wave in the incident bar, and ε_t is the transmitted strain wave in the transmitter bar. Accordingly, the average strain rate and the average stress in the specimen are,

$$\dot{\varepsilon}_s = \frac{V_1 - V_2}{L_s} \tag{5}$$

$$\sigma_s = \frac{F_1 + F_2}{2A_s} \tag{6}$$

where F_1 and F_2 are the forces acting on the two interfaces between the specimen and the incident/transmitter bars, V_1 and V_2 are the particle velocities at the boundary, as shown in Fig. 2, and A_s and L_s are the cross-section area and length of the specimen.

Substituting Eqs. (3) and (4) into (5) and then integrating the strain rate, the strain rate and the strain in the specimen can be obtained as

$$\dot{\varepsilon}_s = \frac{C}{L_s}[(\varepsilon_i - \varepsilon_r) - \varepsilon_t] \tag{7}$$

$$\varepsilon_s = \int_0^t \dot{\varepsilon}_s \, dt = \frac{C}{L_s}\int_0^t [(\varepsilon_i - \varepsilon_r) - \varepsilon_t] dt \tag{8}$$

According to equilibrium condition, it has

$$\sigma_s A_s = \sigma_t A_b \tag{9}$$

where σ_s is the stress in the specimen, σ_t is the stress in the transmitter bar, and A_b is the cross-section area of the bar.

3. Material model for concrete-like material

In the present study, AUTODYN (2005) is adopted to do the numerical simulation of SHPB tests. In AUTODYN, the stress tensor is separated into the hydrostatic tensor and the deviatoric tensor. The hydrostatic stress tensor controls the change of the concrete volume and the deviatoric stress tensor controls the shape deformation.

For the hydrostatic tensor, the hydrostatic pressure p is often related to the density ρ (or volume v) and the internal energy e through an Equation of State (EOS),

$$p = f(\rho, e) \tag{10}$$

The simplest equation of state is linear EOS, that is,

$$p = k\mu \tag{11}$$

where p is the pressure, $\mu = (\rho/\rho_0) - 1$, and K is the material bulk modulus.

The concrete-like material is normally assumed to be a porous material, and the porous equation of state proposed by Herrmann (1969) is used to capture the primary phenomena of them. In Herrmann's P-α model (Herrmann, 1969), the parameter α is determined by,

$$\alpha = \frac{v}{v_s} \tag{12}$$

where v is the specific volume of the porous material and v_s is the specific volume of the material in the solid state at the same pressure and temperature. $v_s = 1/\rho_s$ at zero pressure, and ρ_s is the solid density, that is the density at zero pressure of a fully compacted solid. α becomes unity when the material compacts to a solid. The compaction path, $\alpha(p,e)$, represents the volumetric stiffness of the porous material between the initial compaction pressure p_e and the fully compacted pressure p_s as follows,

$$\alpha = 1 + (\alpha_p - 1)\left[\frac{p_s - p}{p_s - p_e}\right]^n \tag{13}$$

where α_p is the value of α corresponding to the initial plastic yielding, p is the current pressure, n is the compaction exponent, n is assumed to be 3 in the present study.

The deviatoric stress tensor is governed by a damage-based yield strength surface. Before the stress state reaches the yield criterion, the concrete material is assumed to be elastic. The incremental form of the Hooke's law is as follows,

$$\Delta s_{ii} = 2G\left[\Delta\varepsilon_{ii} - \frac{1}{3}\frac{\Delta V}{V}\right]; \quad \Delta s_{ij} = 2G\Delta\varepsilon_{ij} \tag{14}$$

where G is the shear modulus, Δs_{ij} is the deviatoric stress increment, $\Delta\varepsilon_{ij}$ is the strain increment and $\Delta V/V$ is the relative change in volume which can be determined by equation of state.

The strength of the concrete is pressure-sensitive. The yield strength criterion considered is a piece-wise Drucker–Prager model (Zhou et al., 2006), which can be determined by four sets of experimental data: (1) cut off hydro-tensile strength f_{ttt}, ($f_{ttt} = \sigma_1 = \sigma_2 = \sigma_3$); (2) uniaxial tensile strength f_t; ($f_t = \sigma_1$, $\sigma_2 = \sigma_3 = 0$); (3) uniaxial compressive strength f_c ($\sigma_1 = \sigma_2 = 0$,

$\sigma_3 = -f_c$); (4) confined compressive strength ($I_1 = 10\sqrt{3}f_c$, $\sqrt{2J_2} = 6f_c$, where I_1 is the first stress invariant; J_2 is the second deviatoric stress invariant. These values are based on a review of the test results on the compression meridian published in Chen's book (Chen, 1982)). Once the yield surface is reached, the material has permanent plastic strain. The damage scalar D is determined by Mazars' damage model (Mazars, 1986), which is the weighted summation of the tensile and compressive damage as follows,

$$D = A_t D_t + A_c D_c, \quad \dot{D}_t > 0, \quad \dot{D}_c > 0, \quad \text{and} \quad A_t + A_c = 1 \tag{15}$$

The tensile damage D_t and the compressive damage D_c are,

$$D_t(\tilde{\varepsilon}_t) = 1 - e^{-\alpha_t(\tilde{\varepsilon}_t - \varepsilon_{t0})/\varepsilon_{t0}} \quad D_c(\tilde{\varepsilon}_c) = 1 - e^{-\alpha_c(\tilde{\varepsilon}_c - \varepsilon_{c0})/\varepsilon_{c0}} \tag{16}$$

where α_t and α_c are damage parameters and both are taken as 0.5, while ε_{to} and ε_{co} are the threshold strains in uniaxial tensile and compressive states, $\tilde{\varepsilon}_t$ and $\tilde{\varepsilon}_c$ are equivalent tensile and compressive strains, defined as $\tilde{\varepsilon}_t = \sqrt{\sum_{i=1,3}(\varepsilon_i^+)^2}$, $\tilde{\varepsilon}_c = \sqrt{\sum_{i=1,3}(\varepsilon_i^-)^2}$ where ε_i^+ is the positive principal strain. The '+' means it vanishes if it is negative. ε_i^- is the negative principal strain, and the '−' means it vanishes if it is positive. The weights A_t and A_c in Eq. (15) are defined by the following expressions,

$$A_t = \sum_{i=1,3} \frac{H_i[\varepsilon_i^+(\varepsilon_i^+ + \varepsilon_i^-)]}{\tilde{\varepsilon}^2}, \quad A_c = \sum_{i=1,3} \frac{H_i[\varepsilon_i^-(\varepsilon_i^+ + \varepsilon_i^-)]}{\tilde{\varepsilon}^2} \tag{17}$$

where $\tilde{\varepsilon} = \sqrt{\sum_{i=1,3}(\varepsilon_i^+ + \varepsilon_i^-)^2}$ is effective strain. $H_i[x] = 0$ when $x < 0$ and $H_i[x] = x$ when $x \geqslant 0$.

In the strain rate insensitive material model, the DIF caused by the strain rate effect is not considered in the simulations. The simulated strength increase is then caused purely by inertial confinement. In the model, the concrete strength means its static strength.

For comparison, the strain rate sensitive model is also constructed. The compressive DIF adopted here is the typical CEB recommendation (Comite Euro-International du Beton, 1993),

$$\text{CDIF} = \frac{f_{cd}}{f_{cs}} = \left(\frac{\dot{\varepsilon}_d}{\dot{\varepsilon}_{cs}}\right)^{1.026\alpha} \quad \text{for } \dot{\varepsilon}_d \leqslant 30\, s^{-1} \tag{18a}$$

$$\text{CDIF} = \frac{f_{cd}}{f_{cs}} = \gamma(\dot{\varepsilon}_d)^{\frac{1}{3}} \quad \text{for } \dot{\varepsilon}_d > 30\, s^{-1} \tag{18b}$$

where f_{cd} is the dynamic compressive strength at the strain rate $\dot{\varepsilon}_d$ (in the range of 30×10^{-6} to 1000 s^{-1}), $\dot{\varepsilon}_{cs} = 30 \times 10^{-6}$ s^{-1}, $\log\gamma = 6.156\alpha - 0.49$, $\alpha = (5 + 3f_{cu}/4)^{-1}$, f_{cs} is the static compressive strength, and f_{cu} is the static cube compressive strength (in MPa).

The CEB recommendation for the tensile DIF are (Comite Euro-International du Beton, 1993),

$$\text{TDIF} = \frac{f_{td}}{f_{ts}} = \left(\frac{\dot{\varepsilon}_d}{\dot{\varepsilon}_{ts}}\right)^{1.016\delta} \quad \text{for } \dot{\varepsilon}_d \leqslant 30 s^{-1} \tag{19a}$$

$$\text{TDIF} = \frac{f_{td}}{f_{ts}} = \beta\left(\frac{\dot{\varepsilon}_d}{\dot{\varepsilon}_{ts}}\right)^{1/3} \quad \text{for } \dot{\varepsilon}_d > 30 s^{-1} \tag{19b}$$

where f_{td} is the dynamic tensile strength at the strain rate $\dot{\varepsilon}_d$ (in the range of 3×10^{-6} to 300 s^{-1}), f_{ts} is the static tensile strength at the strain rate $\dot{\varepsilon}_{ts}$ ($\dot{\varepsilon}_{ts} = 3 \times 10^{-6}$ s^{-1}), and $\log\beta = 7.11\delta - 2.33$, in which $\delta = 1/(10 + 6f_c'/f_{co}')$, $f_{co}' = 10$ MPa, f_c' is the static uniaxial compressive strength (in MPa).

In the strain rate sensitive model, the concrete strengths are assumed to be the static strengths multiplied by the corresponding empirical DIFs in Eqs. (18) and (19).

4. Numerical simulation of the SHPB test

4.1. Detailed simulation of SHPB test

2D axi-symmetrical numerical model, as shown in Fig. 3, is adopted to simulate the cylinder sample and the pressure bars. The blue area denotes the concrete specimen, and the purple areas are the pressure bars, only part of the bars are

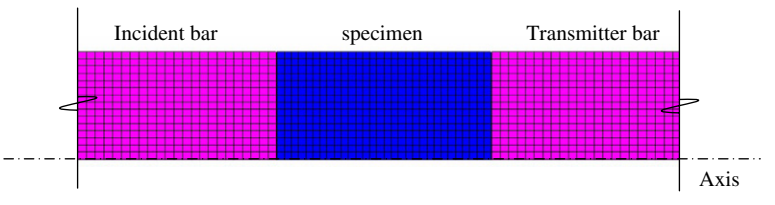

Fig. 3. Numerical model of the specimen and the pressure bars.

shown in the figure. The geometry and the material parameters are assumed to be the same as that in Tedesco et al. (1994). That is, the diameters for the pressure bars and the specimen are 0.0508 m; the length of the specimen is also 0.0508 m, and the length of the pressure bars are 1.3208 m. According to Tedesco's paper (Tedesco et al., 1994), the uniaxial compressive strength of the concrete is 57.7 MPa. The parameters for the concrete are listed in Table 1. The pressure bars was constructed of PH13-8MO stainless steel. The bars are assumed to be elastic, which is true in real case. Typical parameters for steel are adopted in the present simulation, i.e., Young's modulus is 200 GPa, density is 7830kg/m^3, and the Poison's ratio v is 0.3.

In the simulation, stress boundary is set at the left end of the incident bar. The pressure loading shape is trapezium. The stress level is 80 MPa, same as the loading case 2 in Tedesco's paper (Tedesco et al., 1994). The rising time is 23 μs, and the duration is 220 μs. It should be mentioned that the calculated strain rate from the test results is 25 s^{-1} in Tedesco's paper (Tedesco et al., 1994) according to Eq. (7). In the present simulation, gauges are set on the pressure bars and on the specimen as well. The stress-time histories recorded in the incident bars and the transmitter bars from the strain rate-insensitive material model and the strain rate sensitive model are shown in Fig. 4. Comparison of the results from the two different models shows that the maximum transmitted stress obtained from the strain rate sensitive model yields higher dynamic compressive strength for the specimen. Comparison of Fig. 4 and the recorded stress-time history obtained from the test results (Tedesco et al., 1994) shows that the strain rate sensitive model yields better prediction of the test results than the strain rate insensitive model. Especially, as compared with that from the strain rate insensitive model, the shape of the transmitted stress wave from the strain rate sensitive model in Fig. 5 is closer to the test results. However, it should be noted that the dynamic strength of concrete is slightly over-estimated if strain rate sensitive model is used. These observations indicate the strength increase at high strain rates is not caused purely by inertial confinement.

According to Eq. (9), the transmitted stress should be equal to the stress in the specimen because the areas of the specimen and the bars are exactly the same. Fig. 5 shows the stress-time history at the centre point of the specimen from the strain rate insensitive/sensitive material model. Comparison of Fig. 4 and the transmitted stress in Fig. 5 shows that the stress-time histories in the specimen has similar value and shape as that in the transmitted bar. It should be noted that for the current loading case, the simulated stress-time history is almost uniform in the specimen, and the peak value is close to the uniaxial compressive strength of the concrete, that is, 57.7 MPa for the strain rate insensitive model. This numerical result means that no inertial confinement can be found at the strain rate 25 s^{-1} in this loading case (Tedesco et al., 1994). The finding is consistent with other researcher's results (Li and Meng, 2003), where the numerical results showed that there is no obvious strength enhancement when the strain rates are less than 100 s^{-1}. Fig. 5 also shows the stress-time history at the centre point of the specimen from the strain rate sensitive material model, in which the CEB DIF is used. From this figure, it can be found that the calculated dynamic compressive strength is about 73.5 MPa, which is 11.2% higher than the test result of 66.07 MPa.

4.2. Simulation of SHPB test with a simplified model and comparison

To reduce the computational cost, the pressure bars are not included in the simplified numerical model. Instead, only the specimen is considered. The boundary condition for the input surface is set as a velocity boundary, with a trapezium shape; and the velocity is set as zero on the other surface. It should be noted that the present velocity boundary condition is different from the stress boundary condition in the simulation of real SHPB test. However, the stress states in the specimen of the two cases are equivalent, that is, the stress in the specimen increases gradually to reach its strength and then drops to around zero. The simplified method can be found in Ma et al. (2006). Velocity boundary from the test results was also given in Georgin and Reynouard (2003), the test results also lead to similar force boundary conditions. These indicate both force and velocity boundary controlled tests yield similar results. In order to produce the same strain rate for the specimen as in the example described above, i.e., about 25 s^{-1}, and because the length of the specimen is 50.8 mm, the maximum value for the velocity should be 1.27 m/s with the rising time of 23 μs.

The longitudinal stress-time history for a gauge point in the specimen from the strain rate insensitive/sensitive material model is shown in Fig. 6. Comparison of Figs. 5 and 6 shows that the stress response for these different models are similar, especially, the maximum stress obtained is similar, that is, around the concrete uniaxial compressive stress of 57.7 MPa for the strain rate insensitive model. It should be noted that the stress-time history at any point in the specimen is similar to that shown in Fig. 6, which means the specimen under this loading case almost has a uniform stress distribution.

The longitudinal stress-time history for a gauge point in the specimen from the strain rate sensitive material model is also shown in Fig. 6. The calculated strength is about 72 MPa. Comparison of Figs. 5 and 6 also shows that the stress response for

Table 1
Concrete material properties

Parameters for EOS		Parameters for Strength	
Solid density, ρ_s	2.750×10^3 kg/m^3	α_t, α_c	0.5
Initial density, ρ_0	2.405×10^3 kg/m^3	ε_{t0}	2.0e^{-4}
Initial soundspeed, C_0	2.970×10^3 m/s	ε_{c0}	2.0e^{-3}
Initial compaction pressure, p_e	36 MPa	f_t	4.53 MPa
Solid compaction pressure, p_s	6000 MPa	f_c	57.7 MPa
Solid bulk modulus	3.527×10^4 MPa	f_{ttt}	2.5 MPa

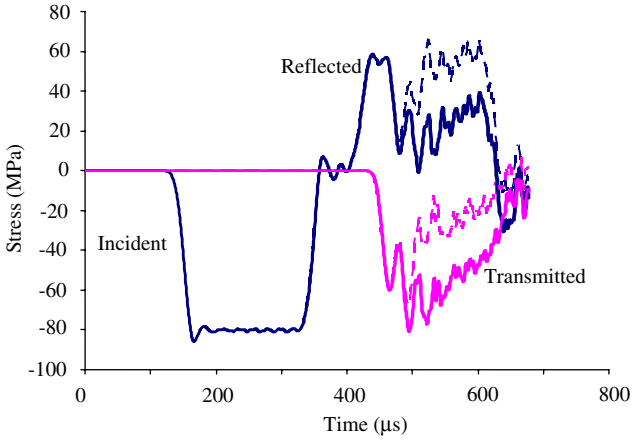

Fig. 4. Numerical results of incident, reflected and transmitted stress (dashed curves are from the strain rate insensitive model, solid curves are from the strain rate sensitive material model).

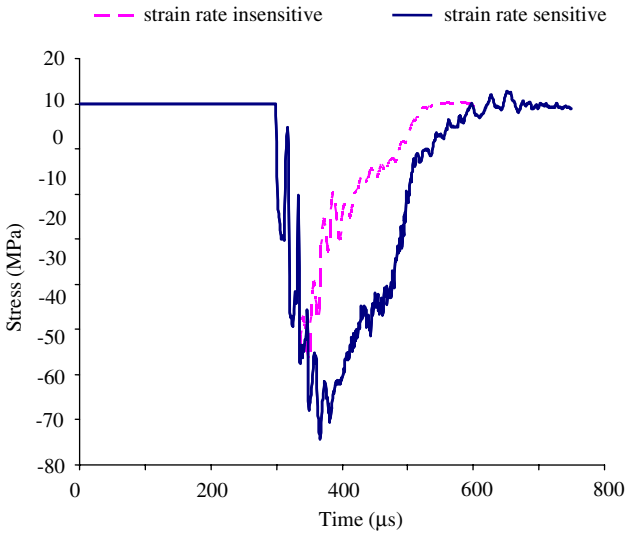

Fig. 5. Numerical results of longitudinal stress in the specimen.

the complicated SHPB model and the simple specimen model are similar. Therefore, the simplified model will be used in the subsequent simulations.

5. Numerical simulation of a specimen under different strain rates

5.1. Homogeneous model

In this section, the simplified model is used to simulate SHPB tests and calculate the dynamic response of concrete-like material specimen under different strain rates. Again, both the strain rate independent and dependent material model described in Section 3 are adopted in the present numerical simulations.

For an ideal SHPB test, the specimen should be in dynamic stress equilibrium (Ravichandran and Subhash, 1994; Song and Chen, 2004). To achieve the dynamic equilibrium at extremely high strain rates, the specimen has to be very small. Thus in the present simulation, a very small specimen is adopted. The same specimen size as in Li and Meng (2003) is used here, i.e., the diameter is 12 mm and the length is 6 mm. The strain rates considered in the present study vary from 21 s^{-1} to 10^4 s^{-1}. For these different strain rates, both the maximum average stresses and the maximum peak stresses of the specimen are analysed. The average stress is obtained by averaging the stress over the entire specimen, while the maximum peak stress denotes the highest stress in the specimen, which always occurs around the centre axis.

In the strain rate insensitive model, both P-α equation of state (EOS) and the linear EOS are used. For the P-α EOS model, the parameters used are listed in Table 1. The bulk modulus for the linear EOS can be calculated as 21 GPa according to the

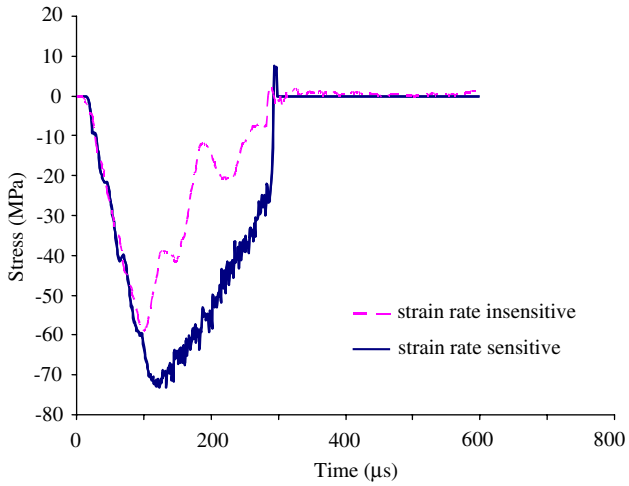

Fig. 6. Numerical results of longitudinal stress in the specimen obtained using the simplified numerical model.

parameters provided in Tedesco et al. (1994). Corresponding to different strain rates, the maximum average stress and the maximum peak stress from the strain rate insensitive model are listed in Table 2. Results from the linear and Porous EOS are listed for comparison. It can be found that the DIFs obtained from the linear EOS are higher than that from the porous EOS when the strain rate is high. It can be also found that the difference between the peak stress and the average stress increases with the increase of the strain rate, which means that the stress distribution is obviously not uniform when it is under high strain rate deformation.

Fig. 7 shows the stress distribution along the radius of the specimen for different strain rate cases when the strain rate insensitive model is used. Position of 0mm corresponds to the centre of the specimen, and the position of 6mm corresponds to the outside free surface. From this figure, it can be clearly seen that the stress in the inner part of the specimen is much higher than that in the outer part in the highest strain rate case. This is not surprise because the inner part has higher pressure, which is due to the inertial confinement. The stresses in Fig. 7 for high strain rate cases show a parabolic distribution, which has the similar shape as the elastic analytical results published in Forrestal et al. (2007). When the strain rate is lower than 200 s^{-1}, the stress distribution over the cross section is almost uniform, indicating the inertial confinement is not obvious, and the dynamic compressive strength is almost equal to the static compressive strength.

5.2. Mesoscale model

Concrete-like material is a highly complex and heterogeneous composite material. The properties of the concrete depend on the properties of its component phases, i.e., aggregate, matrix and the ITZ. Especially, the ITZ plays a critical role in determining the mechanical properties and failure behaviour of concrete composites (Akçaoğlu et al., 2005). Many research works have been done to study the properties of ITZ and its effect on the static mechanical properties of concrete material (AppaRao and RaghuPrasad, 2004; Aquino et al., 1995; Akçaoğlu et al., 2004;Guinea et al., 2002; Zhao and Chen, 1998; Diamond and Huang, 2001; Breugel et al., 2004; Agioutantis et al., 2000).

To obtain more accurate DIFs caused by inertial confinement and to study the failure details of the specimen under dynamic compressive loading, mesoscale model is also used in the present paper. Since the specimen considered is very small, it can only be a kind of mortar, as in many experimental tests (Grote et al., 2001; Jawed et al., 1987).

Table 2
Average peak stress and maximum peak stress versus strain rates

Strain rate (s^{-1})	Maximum average stress (MPa)		Maximum peak stress (MPa)	
	P-α EOS	Linear EOS	P-α EOS	Linear EOS
21.2	57.95	57.38	58.49	57.61
212	61.57	60.78	63.74	63.68
283	62.75	62.57	66.61	66.86
408	65.57	64.89	71.59	71.93
733	72.86	71.20	85.61	85.85
4233	104.95	112.32	180.03	204.7
8467	138.86	169.03	277.65	309.68
10000	157.5	187.81	309.28	347.41

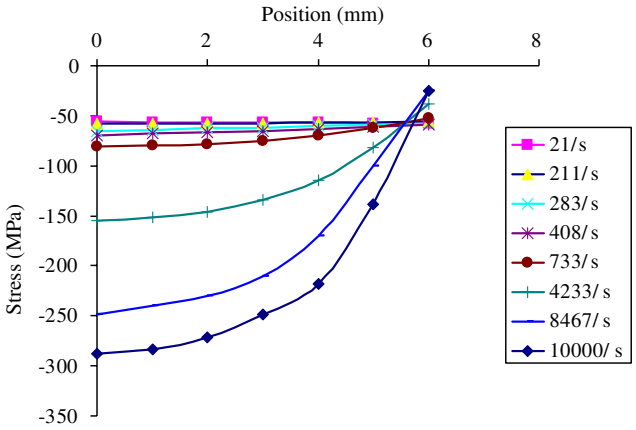

Fig. 7. Stress distribution along the radius of the specimen (strain rate from 21 to 10000 s^{-1}).

In the present mesoscale modelling, the relatively bigger sand particles are modelled as aggregates with higher strength, while the cement paste is assumed to be matrix with lower strength. The interfacial transaction zone (ITZ) is the weakest link between the aggregate and the matrix. Similar method was adopted to simulate the static elastic compressive behaviour of mortar matrix (Agioutantis et al., 2000, 2002), in which the aggregate considered was also sand particle. According to Agioutantis et al. (2000), sand grain distribution is between 1 and 0.125 mm. In the present study, the diameter of the sand grain is assumed to be in the range of 0.5–1.0 mm, and the thickness of the ITZ is assumed to be 50 μm. It should be noted that the properties of the ITZ are not well understood yet, however, it is well accepted that it has large heterogeneity, high porosity and its strength is lower than the matrix. In the strain rate sensitive model, the same material models for the three phases in Zhou and Hao (accepted for publication) are used. P-α EOS (Herrmann, 1969) is used to model both the cement paste and the ITZ, while the linear EOS (Eq. (11)) is used to model the aggregate. The piece-wise linear Drucker–Prager strength model described in Section 3 is used to model all the three phases, with different parameters adopted. The parameters for the three phases are listed in Table 3. The CEB recommendation in Eqs. (17) and (18) for DIFs is used to model the ITZ and the mortar matrix; the DIFs of the aggregate is assumed to be the same as given Zhou and Hao (accepted for publication), which is based on the test results of rock materials (Cho et al., 2003; Wang et al., 2006; Cai et al., 2007; Lok et al., 2003;Li et al., 2004, 2005). The tensile and compressive DIFs are as follows

Table 3
Three-phase mortar material properties

	Mortar marix	ITZ
(a) Material parameters for cement matrix and ITZ		
Solid density, ρ_s (kg/m^3)	2.750×10^3	2.750×10^3
Initial density, ρ_0 (kg/m^3)	2.405×10^3	1.8×10^3
Initial soundspeed C_0 (m/s)	2.970×10^3	2.269×10^3
Initial compaction pressure p_e (MPa)	36	16.2
Solid compaction pressure p_s (MPa)	6000	6000
Shear modulus (GPa)	15.8	4.16
Damage parameters α_t, α_c	0.5	0.5
Tensile damage threshold ε_{st0}	2.0×10^{-4}	2.0×10^{-4}
Compressive damage threshold ε_{sc0}	2.0×10^{-3}	2.0×10^{-3}
Tensile strength, f_t (MPa)	4.53	1.8
Compressive strength, f_c (MPa)	57.7	23
Cut-off tensile strength, f_{ttt} (MPa)	2.5	0.9
(b) Material parameters for sand aggregate		
Density ρ_0 (kg/m^3)		2.750×10^3
Bulk modulus, K (GPa)		35.7
Shear modulus, G (GPa)		17.4
Damage parameters, α_t, α_c		0.5
Tensile damage threshold ε_{st0}		3.6×10^{-4}
Compressive damage threshold ε_{sc0}		3.6×10^{-3}
Tensile strength, f_t (MPa)		15
Compressive strength, f_c (MPa)		200
Cut-off tensile strength, f_{ttt} (MPa)		7.5

$$\text{TDIF} = 0.0225 \log \dot{\varepsilon} + 1.12 \quad \dot{\varepsilon} \leqslant 0.1\ \text{s}^{-1} \tag{20}$$

$$\text{TDIF} = 0.7325(\log \dot{\varepsilon})^2 + 1.235(\log \dot{\varepsilon}) + 1.6 \quad 0.1\ \text{s}^{-1} \leqslant \dot{\varepsilon} \leqslant 50\ \text{s}^{-1} \tag{21}$$

$$\text{CDIF} = 0.0225 \log \dot{\varepsilon} + 1.12 \quad \dot{\varepsilon} \leqslant 10\ \text{s}^{-1} \tag{22}$$

$$\text{CDIF} = 0.2713(\log \dot{\varepsilon})^2 - 0.3563(\log \dot{\varepsilon}) + 1.2275 \quad 10\ \text{s}^{-1} \leqslant \dot{\varepsilon} \leqslant 2000\ s^{-1} \tag{23}$$

The random distribution of the sands is determined by using a Matlab program, in which a series of computer generated random numbers are used to determine the diameters and the positions of the aggregates. The diameters of the sand particles are assumed to vary from 0.5mm to 1mm with a uniform distribution. The placing process can be summarised into the following steps (Wriggers and Moftah, 2006):

Step 1: Random numbers defining the position and the diameter of the aggregate particle are generated.
Step 2: Check whether all the placing conditions are completely satisfied to avoid overlapping of the neighbouring particles or outside the boundary.
Step 3: If a generated particle cannot satisfy the placing condition, new random numbers are generated until all the particles can be properly placed.
Step 4: The steps described above are repeated until a certain area percentage of aggregate is reached.

Fig. 8 shows the numerical model for simulation in AUTODYN. In Fig. 8, different colour areas show different materials, i.e., red areas are sand aggregates, green areas are ITZs and blue area are cement matrix. In the numerical model, the 2D element is a square with the element size of 50 × 50 μm. The geometry of the circular aggregate is only approximately modelled by the square elements.

For two example strain rates, 21 s^{-1} and 10000 s^{-1}, the corresponding longitudinal stress distribution and effective strain are shown in Figs. 9 and 10, respectively. The results from the strain rate sensitive and insensitive models are shown for comparison. In the figures, the effective strain concentration area is used to approximate the "cracks". From Fig. 9(a) of the strain rate insensitive model, it can be found that the ITZ area undergoes high strain first (at the time of 50 μs), then at the time of 100 μs, strain localisation occurs near the free boundary of the specimen. At 150 μs, obvious cracks occur and propagate from the ITZ to the cement matrix; with the development of the cracks, lateral unloading failure wave as mentioned in Bischoff and Perry (1991) travels towards the centre of specimen and the stress near the boundary tends to reach zero. At this time instant, the average stress in the specimen reaches the maximum. Even though obvious cracks can be found, the central part of the specimen can still sustain high stress at the time of 200 μs. At the time of 250 μs, more cracks are generated and the average stress which the specimen can sustain drops gradually. Comparison of Fig. 9(a) and (b) shows that the cracks occur earlier in the strain rate insensitive model, and accordingly the calculated strength is much lower than that of the strain rate sensitive model. It is noticeable that the central part of the specimen undergoes much higher stress and pressure. It should be noted that the present results of the mesoscale model are different from those of the homogeneous model discussed above. In the homogeneous model, the stress distribution along the radius of the specimen is almost uniform at strain rate 21 s^{-1}. From Table 2, it can be found that the maximum stress is only slightly higher than the average stress.

When the strain rate is 10,000 s^{-1}, the maximum average stress occurs at the time of 4.5 μs for the strain rate insensitive model. As shown in Fig. 10(a), at 1 μs, the stress wave travels in the specimen, part of the ITZ and mortar matrix begins to undergo high strain. At 2 and 3 μs, more cracks occur, however, a large area in the centre of the specimen can still sustain high stress. At 5 μs, the stress which the specimen can sustain drops. At the time of 6 μs, the stress in a large area drops to around 0. From Fig. 10(b), it can be clearly seen that much higher stress can be reached when the strain rate sensitive model is adopted.

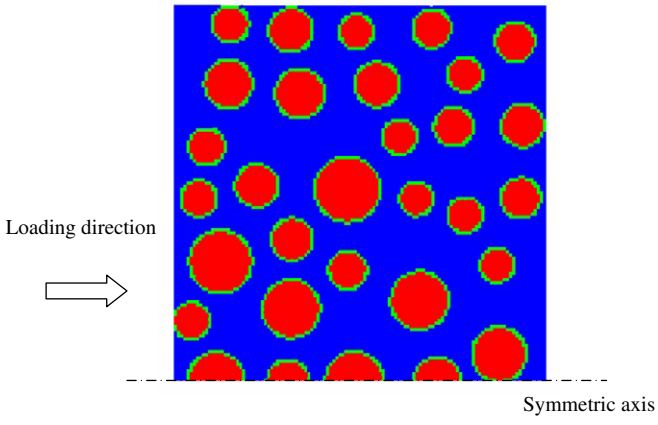

Fig. 8. Three phases in the mesoscale model.

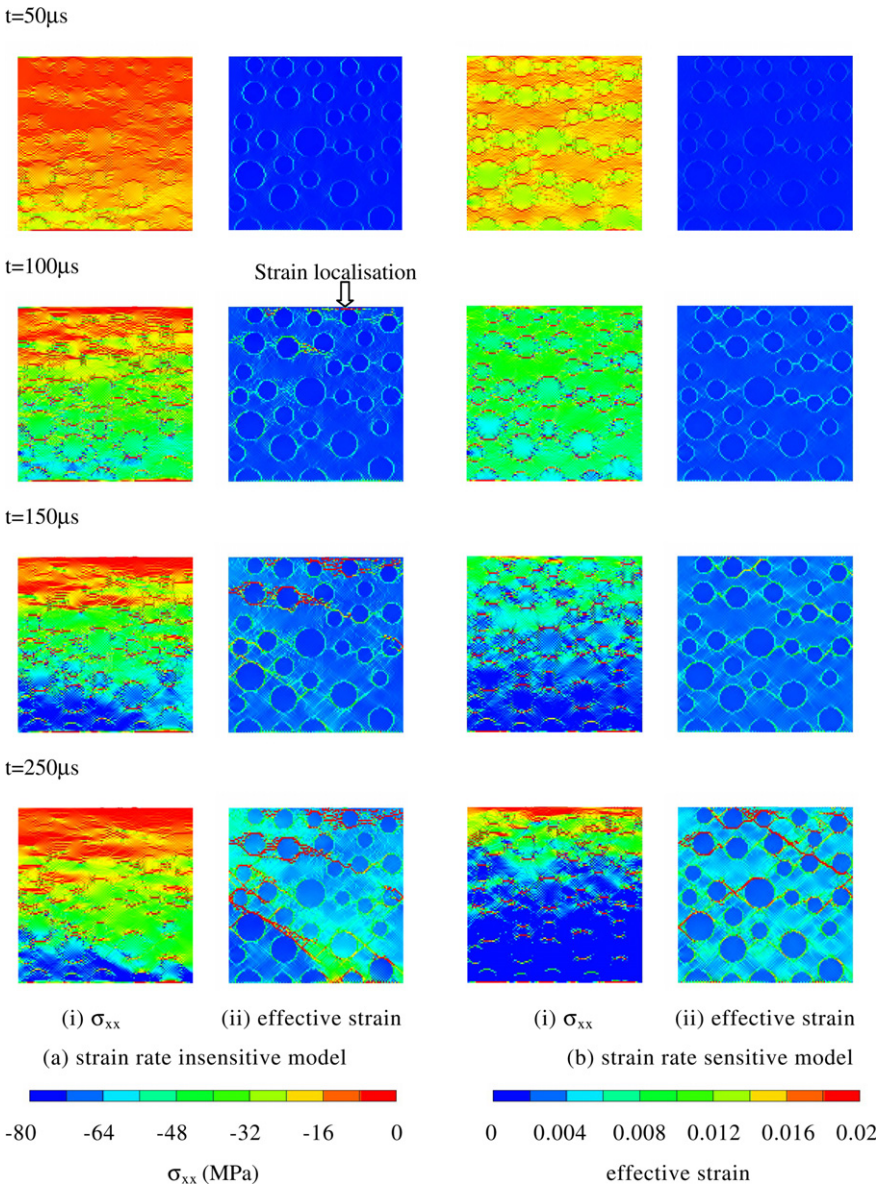

Fig. 9. Stress distribution and effective strain (strain rate = 21 s^{-1}).

Comparison of Figs. 9 and 10 shows that the failure pattern of the high strain rate case is different from that of the low strain rate case. At a low strain rate, only a few big cracks can be found; however at a high strain rate, a lot more cracks are generated. At the high strain rate case as shown in Fig. 10, shear failure are more obvious, many shear cracks are formed at about 45° directions with respect to the loading direction.

5.3. Comparison of numerical results

The DIFs (corresponding to the maximum average stresses) calculated by different numerical models are shown in Fig. 11. In the figure, Homo-NoDIF means that homogenous model is used and strain rate effect is not considered. In Li and Meng (2003), the specimen was also assumed to be homogeneous and strain rate insensitive. There are several differences between their research work and the present study. In their simulation, a detailed numerical model with both incident and transmitted bars together with the specimen was used. However, in our model, a simplified model with only the specimen is calculated. However, the reliability of the simplified model is calibrated. In addition to that, the material model used was different. In Li and Meng's simulation, linear Drucker–Prager model was used to simulate the mortar specimen, while in our model, the piece-wise linear Drucker–Prager model is used to match the experimental results of concrete and mortar. Both the meso-

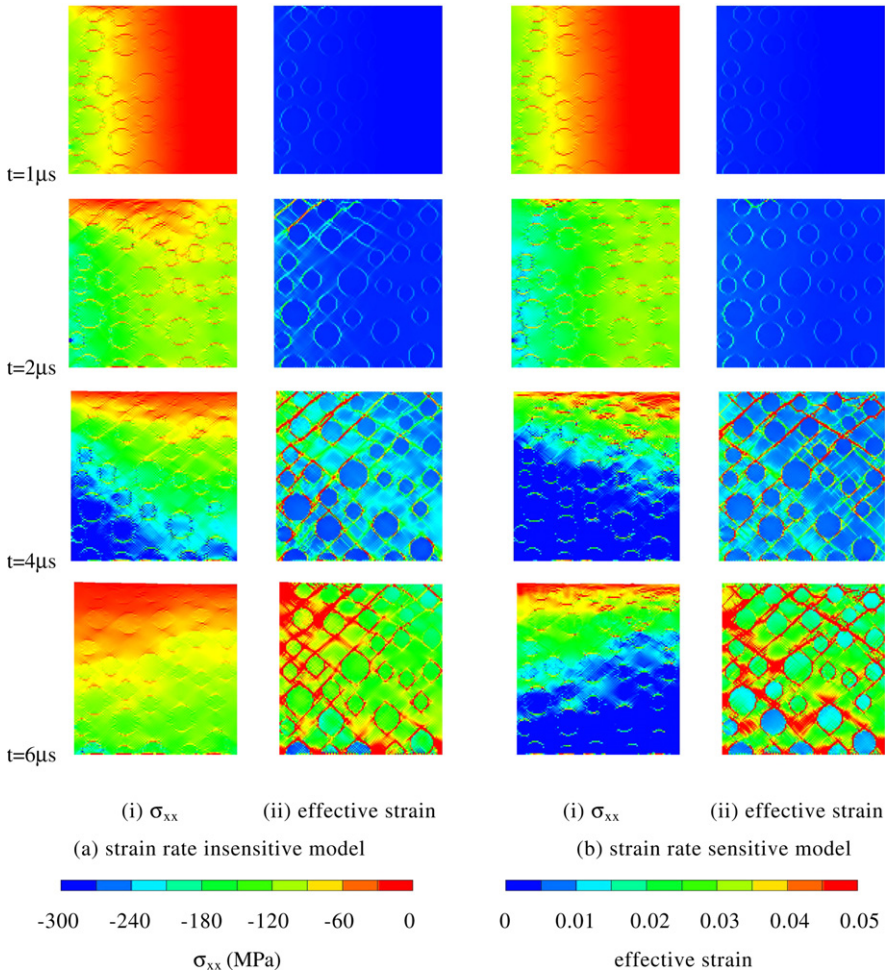

Fig. 10. Stress distribution and effective strain (strain rate = 10,000 s^{-1}).

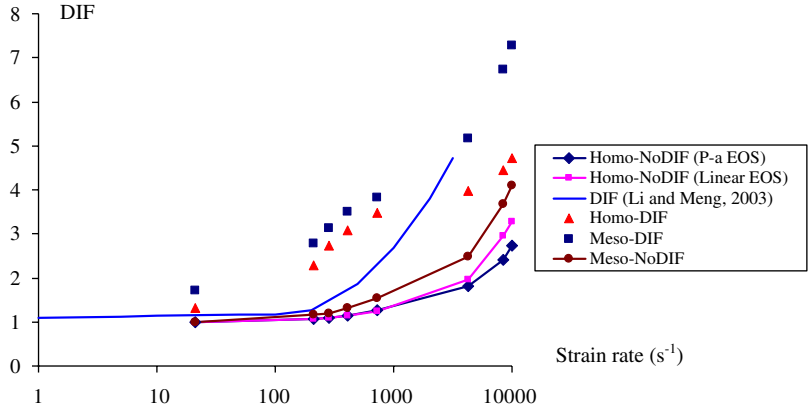

Fig. 11. DIFs obtained from different numerical models.

scale and homogeneous model are used in this study, whereas only a homogeneous model was considered in the previous study. The calculated DIF in Li and Meng (2003) is also shown in Fig. 11. Comparison of the present Homo-NoDIF results and those in Li and Meng (2003) shows that the DIFs caused by the inertial confinement from the two models differ a lot. The DIFs obtained in the present study are much lower than that in Li and Meng (2003). The difference might be caused by the different material models used in the two studies. The linear Drucker–Prager model adopted in Li and Meng (2003) might

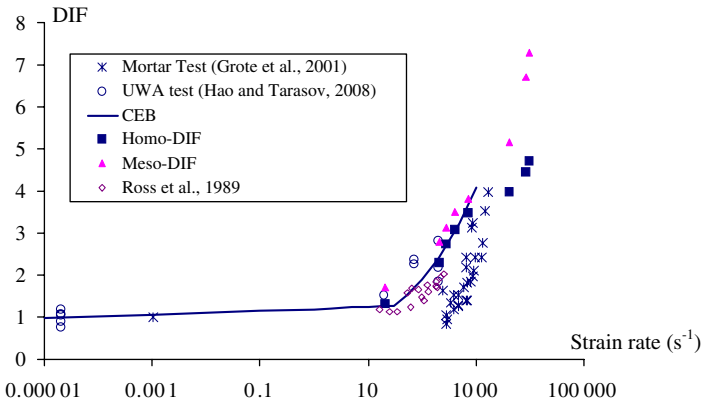

Fig. 12. Comparison of numerical results and some test results.

overestimate the concrete strength when it is under high pressure. In the present study, the piece-wise linear Drucker–Prager model is adopted, which is based on extensive experimental results. Nevertheless, the transition points observed in the present study and that in Li and Meng (2003) are similar, that is, around 200 s^{-1}. That means the inertial confinement is negligible when the strain rate is less than 200 s^{-1}. Extensive test results (Bischoff and Perry, 1991) show that the concrete material already has strain rate enhancement when it undergoes strain rate less than 200 s^{-1}, indicating the importance of material strain rate effect. Therefore, the dynamic compressive strength increase should be a combination of the material strain rate effect and the inertial confinement effect.

Most of the empirical DIFs, such as the CEB recommendation for DIF, are for the strain rate less than 1000 s^{-1}. From the present numerical results shown in Fig. 11, it can be found that the inertial confinement becomes more significant only when the strain rate is higher than 1000 s^{-1}, however, this strain rate is the cut-off value for most strain rate dependant material models for concrete, such as the model in Zhou et al. (2006). The consideration can be assumed reasonable because the compressive strength enhancement for the strain rate higher than 1000 s^{-1} can be assumed to be mainly caused by inertial confinement, whereas the contribution of the material behaviour may be more obvious when the strain rate is lower than 1000 s^{-1}.

The DIFs caused by inertial confinement from the strain insensitive model are also obtained from the mesoscale model, which is marked as Meso-NoDIF. The mesoscale results are also shown in Fig. 11 and compared with the homogeneous model. From the figure, it can be found that the mesoscale model yields higher DIFs than the homogenous model, which means the inertial confinement is more obvious for the mesoscale model than the homogeneous model. This is because the failure mechanism is not the same for the two models. The failure is only caused by pure compression in homogeneous model, while obvious cracks can be found between the aggregates in the mesoscale model. However, the transition points (where the DIFs change dramatically) from both models are the same, that is, around 200 s^{-1}.

For comparison, the DIFs calculated from the strain rate sensitive homogenous model and mesoscale model are shown in Fig. 11 as well, marked as Homo-DIF and Meso-DIF, respectively. Comparison of the present numerical results and some test results and CEB recommendation is shown in Fig. 12. It can be found that the numerical results from both the homogeneous

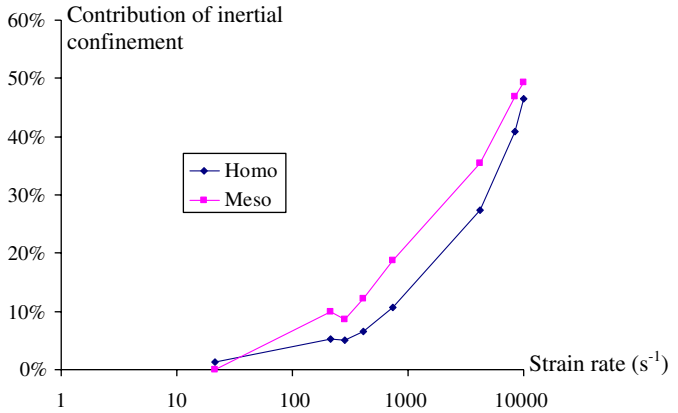

Fig. 13. Contribution of inertial confinement.

and mesoscale model agree well with the CEB recommendation when the strain rate is under 1000 s^{-1}. The results also match the data from the UWA test (Hao and Tarasov, 2008) and the results in Ross et al. (1989). However, the present results over-estimate the test results from Grote et al. (2001).

The contribution percentages of the inertial confinement for both the homogeneous model and the mesoscale model are shown in Fig. 13. From this figure, it can be found that the contribution of the inertial confinement becomes more significant when the strain rate is higher than 200 s^{-1}. It can also be found that the contribution of the inertial confinement is more obvious in the mesoscale model than in the homogeneous model. It should be mentioned that the inertial confinement depends on the specimen size, this effect should be more obvious when the specimen size is bigger. Big size concrete specimen was calculated in our other study in Zhou and Hao (accepted for publication), it was found that the inertial effect is more obvious for bigger size specimen when the strain rate is higher than 200 s^{-1}. However, the inertial confinement was also found to be negligible when the strain rate is lower than 200 s^{-1}.

6. Conclusions

In the present paper, both the homogeneous model and the mesoscale model have been developed to analyse the concrete-like material under high strain rate compression. Comparison of the numerical results from the strain rate sensitive material model and test results shows good agreement. The present numerical results indicate that the inertial confinement does affect the average compressive strength of the specimen. This finding supports other researcher's results (Li and Meng, 2003). However, it is also found that the transition point (from where the DIFs begin to change dramatically) obtained from the present study is about 200 s^{-1}. It means that the inertial confinement is negligible and DIF is mainly caused by material strain rate effect when strain rate is less than 200 s^{-1}. Comparison of the DIFs caused by inertial confinement and the DIFs obtained from dynamic tests shows that the inertial confinement is only one of the two sources that contribute to the DIF, and this contribution becomes more significant when the strain rate is higher than 1000 s^{-1}. Material strain rate effect cannot be neglected in modelling concrete material response to high-rate loadings, especially when the strain rate is less than 200 s^{-1}.

The failure process of concrete specimen is also analysed in a mesoscale model. It is found that the first crack always occurs at the ITZ zone because it is the weakest link between the aggregate and the matrix.

Acknowledgement

The authors wish to acknowledge financial support from the Australian Research Council (ARC) under Grant No. DP0774061 for carrying out this research work.

References

Agioutantis, Z., Chatzopoulou, E., Stavroulaki, M., 2000. A numerical investigation of the effect of the interfacial zone in concrete mixtures under uniaxial compression: the case of the dilute limit. Cement and Concrete Research 30, 715–723.

Agioutantis, Z., Stiakakis, C., Kleftakis, S., 2002. Numerical simulation of the mechanical behaviour of epoxy based mortars under compressive loads. Computers and Structures 80, 2071–2084.

Akçaoğlu, T., Tokyay, M., Çelik, T., 2004. Effect of coarse aggregate size and matrix quality on ITZ and failure behaviour of concrete under uniaxial compression. Cement & Concrete Composite 26, 633–638.

Akçaoğlu, T., Tokyay, M., Çelik, T., 2005. Assessing the ITZ microcracking via scanning electron microscope and its effect on the failure behaviour of concrete. Cement and Concrete Research 35, 358–363.

Appa Rao, G., Raghu Prasad, B.K., 2004. Influence of type aggregate and surface roughness on the interface fracture properties. Materials and Structures 37, 328–334.

Aquino, M.J., Li, Z., Shah, S.P., 1995. Mechanical properties of the aggregate and cement interface. Advanced Cement Based Material 2, 211–223.

AUTODYN, 2005. Century Dynamics, Theory Manual.

Bischoff, P.H., Perry, S.H., 1991. Compression behaviour of concrete at high strain rates. Materials and Structures 24, 425–450.

Breugel, K.V., Koenders, E.A.B., Guang, Y., Lura, P., 2004. Modelling of transport phenomena at cement matrix – aggregate interfaces. Interface Science 12, 423–431.

Cai, M., Kaiser, P.K., Sourineni, F., Su, K., 2007. A study on the dynamic behaviour of the Meuse/Haute-Marne argillite. Physics and Chemistry of the Earth 32, 907–916.

Chen, W.F., 1982. Plasticity in Reinforced Concrete. McGraw Hill, New York.

Cho, S.H., Ogata, Y., Kaneko, K., 2003. Strain-rate dependency of the dynamic tensile strength of rock. International Journal of Rock Mechanics and Mining Science 40, 763–777.

Comite Euro-International du Beton, 1993. CEB-FIP Model Code 1990, Redwood Books, Trowbridge, Wiltshire, UK.

Cotsovos, D.M., Pavlović, M.N., 2007. Numerical investigation of concrete subjected to high rates of uniaxial tensile loading. International Journal of Impact Engineering. doi:10.1016/j.ijimpeng.2007.03.006.

Diamond, S., Huang, J., 2001. The ITZ in concrete – a different view based on image analysis and SEM observations. Cement & Concrete Composites 21, 179–188.

Forrestal, M.J., Wright, T.W., Chen, W., 2007. The effect of radial inertia on brittle sample during the split Hopkinson pressure bar test. International Journal of Impact Engineering 34, 405–411.

Georgin, J.F., Reynouard, J.M., 2003. Modeling of structures subjected to impact: concrete behaviour under high strain rate. Cement and Concrete Composites 25, 131–143.

Grote, D.L., Park, S.W., Zhou, M., 2001. Dynamic behaviour of concrete at high strain rates and pressure: I. Experimental characterization. International Journal of Impact Engineering 25, 869–886.

Guinea, G.V., El-Sayed, K., Rocco, C.G., Elices, M., Planas, J., 2002. The effect of the bond between the matrix and the aggregate on the cracking mechanism and fracture parameters of concrete. Cement and Concrete Research 32, 1961–1970.

Hao, H., Tarasov, B., 2008. Experimental study of dynamic material properties of clay brick and mortar at different strain rates. Australian Journal of Structural Engineering 8 (2).
Herrmann, W., 1969. Constitutive equation for the dynamic compaction of ductile porous materials. Journal of Applied Physics 40, 2490–2499.
Jawed, I., Childs, G., Ritter, A., Winzer, S., 1987. High-strain-rate behaviour of hydrated cement pastes. Cement and Concrete Research 17, 433–440.
Katayama, M., Itoh, M., Tamura, S., Beppu, M., Ohno, T., 2007. Numerical analysis method for the RC and geological structures subjected to extreme loading by energetic materials. International Journal of Impact Engineering 34 (9), 1546–1561.
Kolsky, H., 1949. An investigation of the mechanical properties of materials at very high rates of loading. Proceedings of the Physical Society, Section B 62 (11), 676–700.
Li, H.B., Zhao, J., Li, J.R., Liu, Y.Q., Zhou, Q.C., 2004. Experimental studies on the strength of different rock types under dynamic compression. International Journal of Rock Mechanics and Mining Science. 41(3), Paper 1A 12 – SINOROCK2004 Symposium.
Li, Q.M., Meng, H., 2003. About the dynamic strength enhancement of concrete-like materials in a split Hopkinson pressure bar test. International Journal of Solids and Structures 40, 343–360.
Li, X.B., Lok, T.S., Zhao, J., 2005. Dynamic characteristics of granite subjected to intermediate loading rate. Rock Mechanics and Rock Engineering 38 (1), 21–39.
Lok, T.S., Zhao, P.J., Li, X.B., Lim, C.H., 2003. Dynamic stress–strain response of granite from split Hopkinson Pressure Bar tests. In: Proceedings of the 5th Asia-Pacific Conference on Shock and Impact Loads on Structures, November 12–14, 2003, Changsha, Hunan, China. pp. 277–286.
Ma, G.W., Dong, A., Li, J., 2006. Modeling strain rate effect for heterogeneous brittle materials. In: First International Conference on Analysis and Design of Structures against Explosive and Impact Loads, September 15–17, 2006, Tianjin, China. Transaction of Tianjin University, 12 (Suppl.), pp. 79–82.
Mazars, J., 1986. A description of micro- and macroscale damage of concrete structures. Engineering Fracture Mechanics 25, 729–737.
Ravichandran, G., Subhash, G., 1994. Critical appraisal of limiting strain rates for compression testing of ceramics in a split Hopkinson pressure bar. Journal of the American Ceramic Society 77, 263–267.
Ross, C.A., Thompson, P.Y., Tedesco, J.W., 1989. Split-Hopkinson pressure-bar tests on concrete and mortar in tension and compression. ACI Materials Journal 86-M43, 475–481.
Song, B., Chen, W., 2004. Dynamic stress equilibrating process in a rubber specimen during a split Hopkinson pressure bar experiment. Experimental Mechanics 44 (3), 300–312.
Tedesco, J.W., Hughes, M.L., Ross, C.A., 1994. Numerical simulation of high strain rate concrete compression tests. Computers and Structures 51 (1), 65–77.
Tedesco, J.W., Ross, C.A., 1998. Strain-rate-dependent constitutive equations for concrete. Journal of Pressure Vessel Technology – Transactions of the ASME 120 (4), 398–405.
Wang, Q.Z., Li, W., Song, X.L., 2006. A method for testing strength and elastic modulus of rock materials using SHPB. Pure and Applied Geophysics 163, 1091–1100.
Wriggers, P., Moftah, S.O., 2006. Mesoscale models for concrete: homogenisation and damage behaviour. Finite Elements in Analysis and Design 42, 623–636.
Zhao, X.H., Chen, W.F., 1998. Effective elastic moduli of concrete with interface layer. Computers & Structures 66, 275–288.
Zhou, X.Q., Hao, H., accepted for publication. Mesoscale modelling of compressive behaviour of concrete at high strain rate. In: Proceedings of the Australian Structural Engineering Conference, June 26–27, 2008.
Zhou, X.Q., Hao, H., Kuznetsov, V.A., Waschl, J., 2006. Numerical calculation of concrete slab response to blast loading. In: First International Conference on Analysis and Design of Structures against Explosive and Impact Loads, September 15–17, 2006, Tianjin, China. Transaction of Tianjin University, 12 (Suppl.), pp. 94–99.